

Direct Numerical Simulation of 2-D and 3-D Instability Waves in a Laminar Separation Bubble

Ulrich Rist

Ulrich Maucher

Institut für Aerodynamik und Gasdynamik

Universität Stuttgart

Pfaffenwaldring 21

70550 Stuttgart

Germany

1. SUMMARY

Direct Numerical Simulations of a laminar separation bubble are presented, where the bubble is generated by prescribing a locally decelerated free-stream velocity along a flat-plate. Controlled disturbances are introduced into the flow field upstream of the bubble by suction and blowing through the wall in order to study the linear and nonlinear stability characteristics of the flow. A number of generic cases with different two-dimensional (*2-D*) and three-dimensional (*3-D*) initial disturbance amplitudes are investigated, (i) a linear case, (ii) a case subject to secondary instability (strong amplification of 3-D disturbances by resonance with a large amplitude 2-D wave), (iii) a 3-D nonlinear case (interaction of two oblique waves), and (iv) a nonlinear case combining the interaction of two oblique waves with a 2-D wave. Good quantitative agreement of the numerical results with (local) linear stability theory is observed throughout case (i) and for the initial disturbance development of the priming waves in the other cases despite the nonparallel base flow. For the nonlinear disturbance development, however, unexpected results are obtained: Secondary instability is hard to distinguish from primary instability and apparently breaks down as soon as the priming 2-D disturbances saturate. However, the nonlinear mechanism identified in cases (iii) and (iv), is obviously much more likely to produce large amplitude 3-D disturbances necessary for the generation of a transitional laminar separation bubble. The mechanism leads to a nonlinearly saturated regime with reasonably turbulent mean-flow characteristics as well as longitudinal vortices in the reattachment zone.

2. INTRODUCTION

Laminar separation bubbles may occur at low Reynolds number under certain operating conditions, especially on laminar-flow airfoils (cf. [1]). Due to a strong adverse pressure gradient downstream of the minimum pressure point the laminar boundary layer may separate before undergoing transition. Most separation bubbles are transitional, i.e., the bubble is closed by turbulent reattachment. Improving flight and performance characteristics of laminar-flow airfoils and compressor blades requires an accurate prediction of separation bubbles. However, all present models used for the prediction of separation bubbles rely on empirical relations derived from experiments, since the flow physics are not yet fully understood. Turbulence models good enough for predicting transitional flows are not available and most Direct Numerical

Simulations (*DNS*) of laminar separation bubbles are, so far, only based on the 2-D Navier-Stokes equations. 2-D investigations were justified due to the observation of 2-D effects dominating the flow in the separation zone and inside the bubble. For the generation of turbulence, however, 3-D effects are necessary. In addition, longitudinal vortices have been observed in some experiments (e.g., [2]) in the reattachment zone behind the bubble.

The present work is a continuation of earlier (2-D) investigations by Gruber et al. [3] (2-D) and Rist [4] (3-D) with the aim of obtaining deeper insight into the transition and reattachment process in laminar separation bubbles. Based on the experience gained from the DNS of flat-plate boundary-layer transition [5] where transition in a low turbulence environment is initiated by a sequence of instabilities, e.g., primary instability (instability of the base flow versus Tollmien-Schlichting waves) and secondary instability (instability of the flow in the presence of finite-amplitude 2-D waves versus small amplitude 3-D disturbances), a number of generic disturbance combinations are investigated in the present paper.

3. NUMERICAL METHOD

Only a general outline of the method will be given here, details are available in [5] – [9]. The latest version of the DNS-scheme developed by Fasel et al. [5], improved by Kloker et al. [6] and more recently by Kloker [7], is used. It is based on the numerical solution of the complete 3-D Navier-Stokes equations in vorticity-velocity formulation for incompressible unsteady flow. The flow is split into a two-dimensional steady base flow and a three-dimensional unsteady disturbance flow in such a way that *no* linearization occurs. This allows the calculation of different base flows by prescribing different free-stream velocity distributions without altering the boundary conditions for the calculation of the disturbance flow. Thus, compared to earlier simulations of boundary layer instability and transition, only the base flow had to be changed for the calculations presented in this paper.

3.1 Governing equations

The flow over a flat plate is considered (see Figure 1) where the streamwise, wall normal, and spanwise directions are denoted by x , y , and z , respectively with their relevant velocity components denoted by u , v , and w . All variables are nondimensionalized by the free-stream velocity \overline{U}_∞ upstream of the separation bubble and by a reference length \overline{L} , where overline denotes dimensional variables

$$\begin{aligned} x &= \frac{\overline{x}}{\overline{L}}, & y &= \sqrt{Re} \frac{\overline{y}}{\overline{L}}, & z &= \frac{\overline{z}}{\overline{L}}, \\ u &= \frac{\overline{u}}{\overline{U}_\infty}, & v &= \sqrt{Re} \frac{\overline{v}}{\overline{U}_\infty}, & w &= \frac{\overline{w}}{\overline{U}_\infty}, \end{aligned} \quad (1)$$

and $Re = \overline{U}_\infty \overline{L} / \overline{\nu}$ is the global Reynolds number. For all investigations presented here, $Re = 10^5$ ($\overline{U}_\infty = 30 \text{ m/s}$, $\overline{\nu} = 1.5 \cdot 10^{-5} \text{ m}^2/\text{s}$, and $\overline{L} = 0.05 \text{ m}$).

With the vorticity defined as $\vec{\omega} = -rot(\vec{u})$, the vorticity

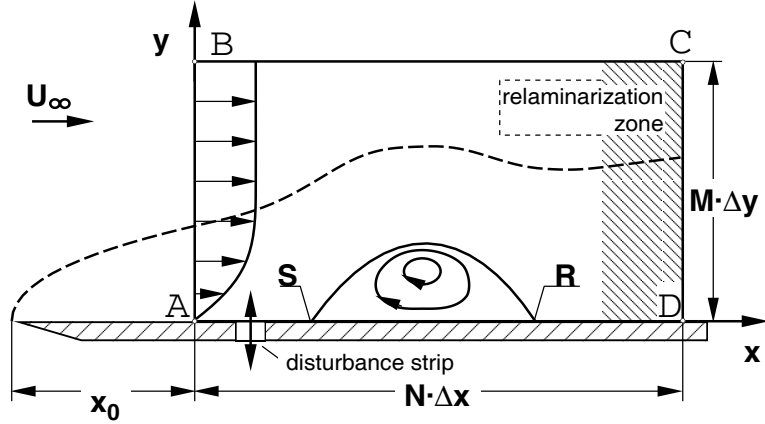


Figure 1: Integration domain for the DNS of a laminar separation bubble. S = separation point, R = reattachment point.

transport equations for the calculation of the x-, y-, and z-vorticity components are

$$\begin{aligned}
\frac{\partial \omega_x}{\partial t} + \frac{\partial}{\partial y}(v\omega_x - u\omega_y) - \frac{\partial}{\partial z}(u\omega_z - w\omega_x) &= \tilde{\Delta}\omega_x, \\
\frac{\partial \omega_y}{\partial t} - \frac{\partial}{\partial x}(v\omega_x - u\omega_y) + \frac{\partial}{\partial z}(w\omega_y - v\omega_z) &= \tilde{\Delta}\omega_y, \\
\frac{\partial \omega_z}{\partial t} + \frac{\partial}{\partial x}(u\omega_z - w\omega_x) - \frac{\partial}{\partial y}(w\omega_y - v\omega_z) &= \tilde{\Delta}\omega_z,
\end{aligned} \quad (2)$$

where

$$\tilde{\Delta} = \frac{1}{Re} \frac{\partial^2}{\partial x^2} + \frac{\partial^2}{\partial y^2} + \frac{1}{Re} \frac{\partial^2}{\partial z^2}. \quad (3)$$

The velocity components are calculated from

$$\begin{aligned}
\frac{\partial^2 u}{\partial x^2} + \frac{\partial^2 u}{\partial z^2} &= -\frac{\partial \omega_y}{\partial z} - \frac{\partial^2 v}{\partial x \partial y}, \\
\tilde{\Delta} v &= \frac{\partial \omega_x}{\partial z} - \frac{\partial \omega_z}{\partial x}, \\
\frac{\partial^2 w}{\partial x^2} + \frac{\partial^2 w}{\partial z^2} &= \frac{\partial \omega_y}{\partial x} - \frac{\partial^2 v}{\partial y \partial z}.
\end{aligned} \quad (4)$$

Next, the flow is split into a steady, two-dimensional base flow (index B), and an unsteady, three-dimensional disturbance flow (denoted by primes)

$$\begin{aligned}
u &= u_B + u', & v &= v_B + v', & w &= w', \\
\omega_x &= \omega'_x, & \omega_y &= \omega'_y, & \omega_z &= \omega_{zB} + \omega'_z.
\end{aligned} \quad (5)$$

Inserting equation (5) into equations (2 – 4) and sorting out the equations to be fulfilled by the base flow yields two sets of equations for the calculation of the base and for the disturbance flow, respectively. The boundary conditions are split

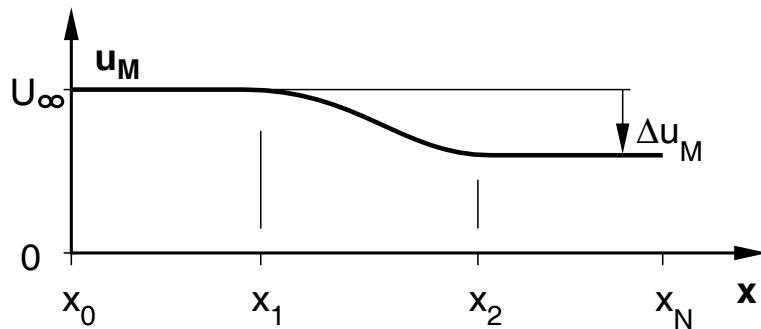


Figure 2: Velocity distribution along the free-stream boundary of the integration domain.

accordingly, and both flows are computed separately, as described in the next two sections.

3.2 Calculation of the base flow

The integration domain is divided into N and M equally spaced intervals in x and y direction, as shown in Figure 1. Blasius boundary layer profiles are prescribed at the inflow boundary A–B, the no-slip boundary condition applies at the plate’s surface at $y = 0$, and at outflow (C–D) the governing equations are solved with the assumption of $1/Re \cdot \partial^2 f / \partial x^2 = 0$, where $f = [u_B, v_B, \omega_{zB}]$. The “relaminarization zone” and the “disturbance strip” shown in Figure 1 are not used for the calculation of the base flow. Along the upper boundary B–C a free-stream velocity distribution is prescribed containing a smooth step by Δu_M between x_1 and x_2 (cf. Figure 2). A steady finite difference solution to the 2-D base flow equations is sought by using an $\mathcal{O}(\Delta x^4, \Delta y^4, \Delta t^2)$ -accurate finite difference x-implicit, y-explicit splitting method.

3.3 Calculation of the disturbance flow

After the base flow has been calculated, disturbances are introduced into the integration domain by timewise periodic blowing and suction upstream of the bubble within the “disturbance strip”, and their downstream development is obtained by solving the 3-D disturbance flow equations.

Periodicity in spanwise direction is assumed, and an effective pseudospectral/finite difference scheme is constructed by using a Fourier ansatz in z -direction

$$f(x, y, z, t) = \sum_{k=-K}^K F_k(x, y, t) e^{ik\gamma z}, \quad (6)$$

where $f = [u', v', w', \omega'_x, \omega'_y, \omega'_z]$, $F_k = [U_k, V_k, W_k, \Omega_{xk}, \Omega_{yk}, \Omega_{zk}]$, and $\gamma = 2\pi/\lambda_z$ is the spanwise wave number. Since f in equation 6 is a real quantity, only those modes with $k \geq 0$ need to be calculated, the others are defined by $F_{-k} = \overline{F_k}$, where $\overline{}$ stands for the complex conjugate. $\mathcal{O}(\Delta x^4, \Delta y^4)$ -accurate finite difference expressions are used for discretization on the grid already used in section 3.2 for the calculation of the base flow. Time integration is performed by an explicit,

$\mathcal{O}(\Delta t^4)$ -accurate four stage Runge-Kutta scheme using central, upwind, downwind, and again central finite differences for the x-convection terms, in each stage, respectively. The sequence of upwind and downwind differences is altered for every time step. It can be shown that this technique effectively damps out small scale oscillations that cannot be accurately discretized on a given grid [7].

The boundary conditions for the disturbance flow are: no disturbances at inflow (A-B), no slip at the plate (A-D), except for the wall-normal velocity within the disturbance strip

$$V_k(x, 0, t) = A_k \sqrt{Re} v_w(x) \sin(\beta t), \quad (7)$$

where $v_w(x)$ is a “wall-forcing function”, and β is the dimensionless frequency related to the frequency parameter $F = \overline{\beta v} / \overline{U}_\infty^2 \cdot 10^4$ usually used in boundary-layer stability theory by $\beta = F \cdot Re \cdot 10^{-4}$. $v_w(x)$ is zero everywhere, except within the disturbance strip, where a point-symmetric amplitude distribution with respect to the strip’s center is constructed from the 5th-order polynomial $v_w(\xi) = 20.25 \cdot \xi^5 - 35.4375 \cdot \xi^4 + 15.1875 \cdot \xi^3$ with ξ running from 0 to 1 in the first and from 1 to 0 in the second half of the disturbance strip.

The vorticity at the wall is calculated from

$$\begin{aligned} \frac{\partial^2 \omega_x}{\partial x^2} \Big|_{y=0} + \frac{\partial^2 \omega_x}{\partial z^2} \Big|_{y=0} &= -\frac{\partial^2 \omega_y}{\partial x \partial y} \Big|_{y=0} + \frac{\partial}{\partial z} \tilde{\Delta} v \Big|_{y=0}, \\ \omega_y \Big|_{y=0} &= 0, \\ \frac{\partial \omega_z}{\partial x} \Big|_{y=0} &= \frac{\partial \omega_x}{\partial z} \Big|_{y=0} - \tilde{\Delta} v \Big|_{y=0}. \end{aligned} \quad (8)$$

At the upper boundary of the integration domain (B-C) an exponential decay of the disturbances in y-direction is allowed, and hence a relatively small integration domain of only a few boundary layer thicknesses can be used. Starting already upstream of the outflow boundary (C-D), the disturbances are forced to decay by gradual suppression of the disturbance vorticity (with x) [6]. This technique has been carefully tested, it works for boundary layers as well as for strongly nonparallel base flows, like e.g., free shear layers or bluff body wakes.

4. NUMERICAL RESULTS

The integration domain shown in Figure 1 begins at $Re_{\delta_1} = 1.72077 \sqrt{x_0} \cdot Re = 331$, extends over $18\delta_1$ in y-direction (until $y = 18.84$) and from $x_0 = 0.37$ to $x_N = 5.06$. A velocity step by $\Delta u_M = 9\%$ is prescribed between $x_1 = 0.71$ and $x_2 = 2.43$ according to Figure 2. Except where noted, 697 and 96 equally sized intervals are used for discretization in x- and y-direction, respectively for a discretization using approx. 25 grid points per TS-wavelength in x-direction and 100 time steps per period. With the disturbance strip placed between $x = 0.55$ and $x = 0.70$ and the “relaminarization zone” beginning at $x_{rz} = 4.67$, the spanwise wave number in equation (6) is set to $\gamma = 20$.

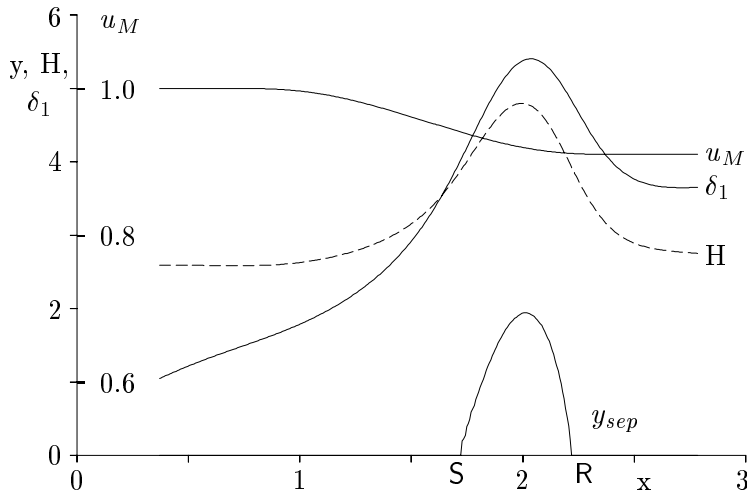


Figure 3: Base flow parameters: free-stream velocity u_M , shape factor H , displacement thickness δ_1 , separation streamline y_{sep} , separation point S , and reattachment point R .

4.1 Base flow

Characteristic features of the base flow are given in Figure 3. They allow the comparison of the prescribed free-stream velocity $u_M(x)$ with the displacement thickness $\delta_1(x)$, the shape factor $H(x)$ (displacement thickness/momentum thickness), and the separation streamline corresponding to $\Psi = 0$ where Ψ is the (2-D) stream function. Here and in all subsequent figures S and R mark the separation and reattachment of the base flow, they are repeated to facilitate comparison between different figures. The shape factor starts with the Blasius value $H = 2.59$ at inflow, increases to a maximum around 4.8, and decreases again in the reattachment region. The strong increase of δ_1 and hence H begins already upstream of the bubble. Separation and reattachment, however, occur downstream of the largest gradient of $u_M(x)$ at those positions where $H \approx 4$. With $\delta_{1S} \approx 4.0$ at separation according to Figure 3, the Reynolds number based on the displacement thickness at separation $Re_{\delta_{1S}} = \sqrt{Re} \cdot \delta_{1S} \approx 1265$ turns out to be quite large compared to the Blasius value of $Re_{\delta_1} = 1.72077\sqrt{x_S \cdot Re} \approx 715$ for the same x . Behind the bubble, the flow asymptotically recovers to a Blasius boundary layer indicating that the laminar separation bubble has primarily a local effect on the base flow. Since δ_1 decreases downstream of the bubble until the decrease is superseded by the growth of the flat-plate boundary layer, Re_{δ_1} would also decrease and the presentation of the results further down, based on a local normalization by δ_1 would be equivocal. It is therefore better to keep to the “global normalization” introduced in equation (1).

4.2 Choice of disturbance frequency

Linear Stability Theory (*LST*) calculations based on the Orr-Sommerfeld equation and using u_B -velocity profiles calculated in the previous section, revealed that the flow was most unstable with respect to 2-D disturbances with frequencies

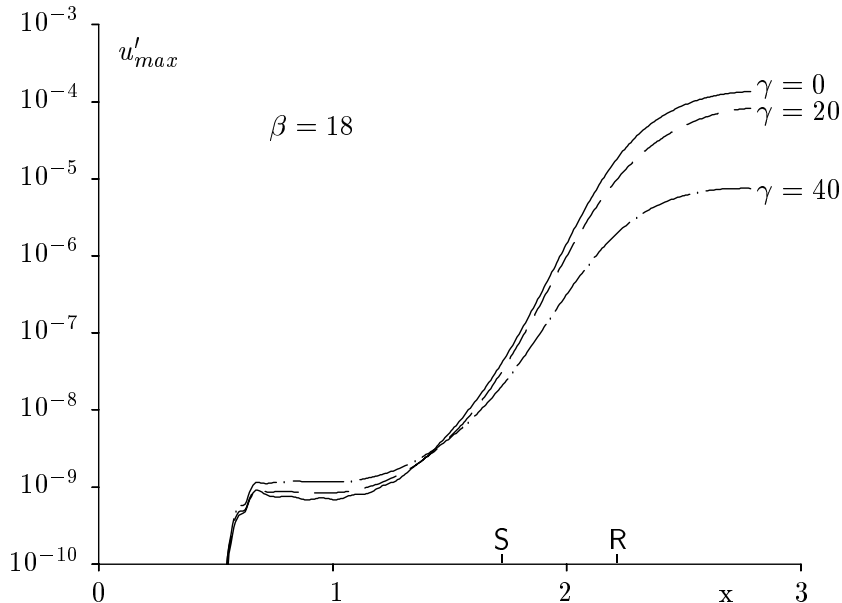


Figure 4: Amplification curves for small-amplitude disturbances (case **L**), $\beta =$ frequency, $\gamma =$ spanwise wave number.

around $\beta = 18$ ($F = \beta/Re \cdot 10^4 = 1.8$ in the stability diagram). This was verified in the DNS with small amplitude wave packets centered at $\beta = 7, 14$, and 28 , respectively. In all three cases the most amplified disturbance occurred at $\beta \approx 18$. The disturbance frequency for all subsequent studies using periodical forcing was therefore set to $\beta = 18$.

4.3 Discussion of Results

Depending on the choice of the disturbance amplitudes A_k in equation (7), different cases can be investigated: a “linear” case (**L**) with a 2-D and two pairs of 3-D TS-waves each with such a small amplitude that no relevant nonlinear interactions occur; a “fundamental” case (**F**) with a large amplitude 2-D TS-wave together with small amplitude 3-D TS-waves; an “oblique” case (**O**), where only one large-amplitude 3-D wave pair is introduced; and a “combined” case (**C**), where an equally large 2-D TS-wave is introduced together with the oblique wave pair of case **O**. In the first two cases, the spectral ansatz (6) is truncated at $K = 2$, and disturbances are introduced for $k = 0, 1$, and 2 , i.e., $\gamma = 0, 20, 40$, respectively. In the other two cases, eqn. (6) is truncated at $K = 4$ or larger.

4.3.1 Linear case

Amplification curves of the u' -disturbance maxima vs. x are shown in Figure 4 for the 2-D wave and the 3-D wave pairs. Generated at the disturbance strip ($0.55 \leq x \leq 0.70$) with $A_0 = A_1 = A_2 = 10^{-10}$ in (7), the waves undergo a strong amplification over several orders of magnitude, starting already upstream of the separation point. The amplification is strongest for the flat wave, it decreases with increasing spanwise wave number. Downstream of the bubble, the amplification is reduced due to the relaxation of the base flow to a Blasius boundary layer. It is important to note that the magnitude of the amplification rate $\alpha_i = -d/dx(\ln u'_{max})$ is

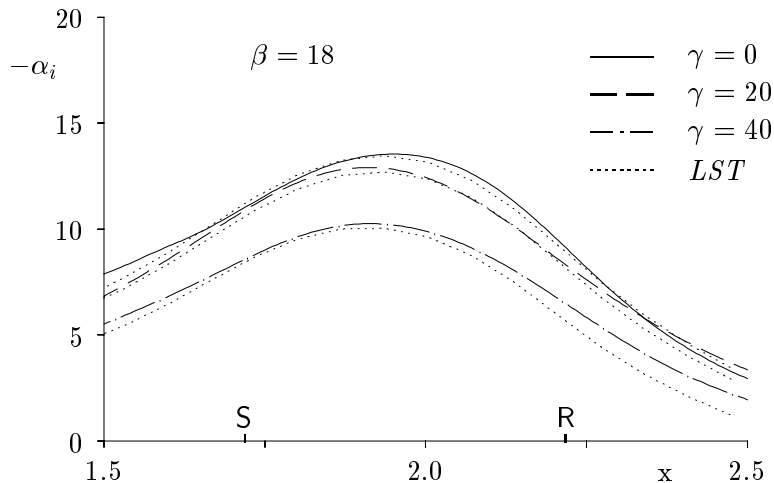


Figure 5: Comparison of DNS-amplification rates from case **L** with Linear Stability Theory (*LST*), β = frequency, γ = spanwise wave number.

more than ten times larger in presence of the bubble than without it. In addition, 3-D waves are nearly as amplified as 2-D waves.

A quantitative comparison of the amplification rates extracted from Figure 4 with results of LST using local base flow profiles, i.e., parallel-flow assumption, is given in Figure 5. Remarkably good quantitative agreement is observed, small differences can be attributed to the nonparallel base flow, since the disturbance amplitudes are too small for nonlinear effects ($\mathcal{O}(10^{-4})$). Closer investigation of these nonparallel effects showed that the v' -disturbance maximum agrees better with LST in the downstream part of the bubble, whereas u'_{max} agrees better in the upstream part. Such qualitative behavior is plausible, since the streamlines have different (concave/convex) curvature before and after the bubble. On the whole, nonparallel effects are surprisingly small.

4.3.2 Fundamental case

The only difference of this case to the previous one is a much larger amplitude of the 2-D wave at the disturbance input, $A_0 = 10^{-5}$ (compare above). The intention is to simulate a combination that will lead to K-type transition in a Blasius boundary layer. In such a case, a tenfold increase of the 3-D amplification rates can be expected due to secondary instability [10]. As long as the amplitudes of the 3-D disturbances are very small, no interaction is expected among these, and the simultaneous introduction of two oblique wave pairs is considered an effective means of getting an idea about the sensitivity of the expected resonance to the spanwise wave number.

Except for the larger amplitude of the 2-D wave, the 2-D and 3-D disturbances in Figure 6 initially develop in the same way as in Figure 4. However, when the 2-D wave attains amplitudes of $u'_{max}/U_\infty \approx 20\%$, nonlinear effects are responsible for its saturation which persists downstream of the bubble. As

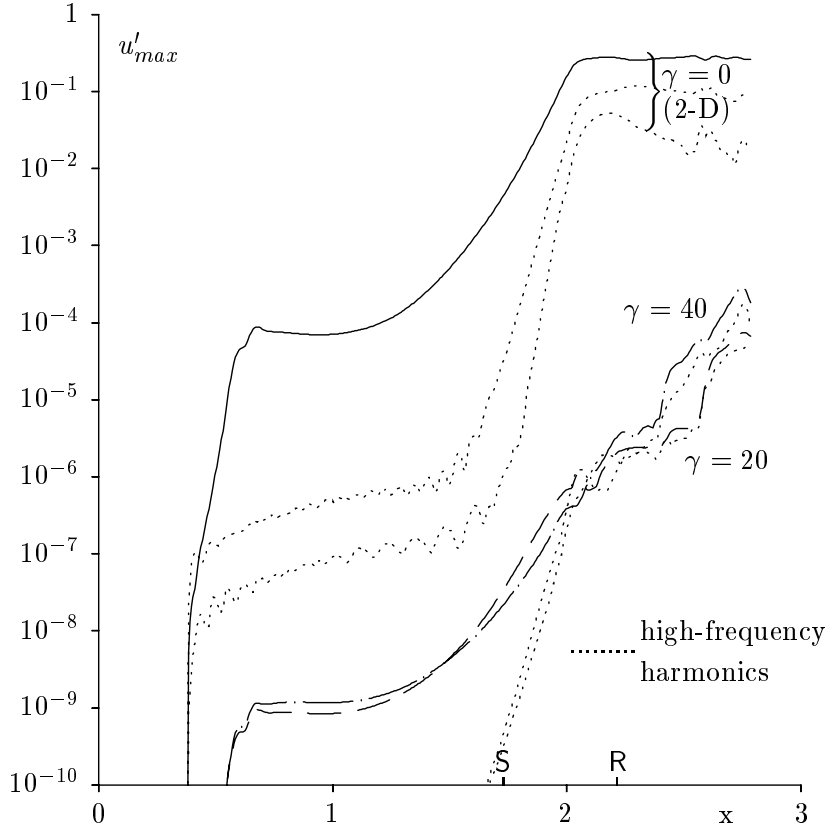


Figure 6: Amplification curves for large 2-D and small 3-D disturbance amplitudes (case **F**), $\gamma =$ spanwise wave number.

already shown in [4] and as will be shown further down, the flow is qualitatively reasonable for $x > 2.0$, despite the possible deterioration of the numerical results due to insufficient numerical resolution for $x > 2.0$.

High-frequency harmonics ($\beta = 36$ and $\beta = 54$ for the 2-D wave, $\beta = 36$ for the 3-D waves) have been included in Fig. 6 as dotted lines in order to give an additional indication of nonlinear effects. Saturation of disturbance amplitudes at a high level and generation of higher harmonics are typical nonlinear phenomena which can also be observed in other base flows, e.g., in a Blasius boundary layer [8], [9]. In case **L**, where no saturation is observed, all higher harmonics stay below 10^{-7} .

As regards the 3-D disturbances, which were supposed to get in resonance with the 2-D wave and strongly amplified by secondary instability (cf. Herbert [10]) after the 2-D wave has attained sufficiently large amplitudes ($\mathcal{O}(1\%)$), an unexpectedly reduced growth of the 3-D waves is observed as soon as the 2-D wave saturates. This could again be due to nonlinear effects since the 3-D higher harmonics shown have approximately the same amplitude as the fundamentals. However, the reduced amplification may also be explained by nonlinear deformation and stabilization of the mean flow due to the action of the 2-D nonlinear disturbances, as already shown in [4].

In order to validate this surprising result, case **F** has been

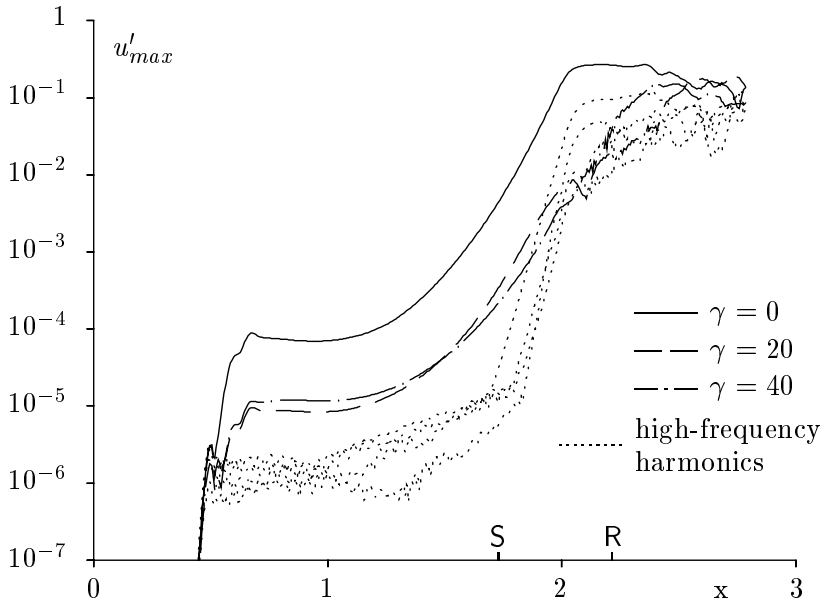


Figure 7: Effect of increasing the 3-D disturbance amplitude compared to Figure 6, $\gamma =$ spanwise wave number.

re-computed using smaller grid sizes in x and time (i.e., ≈ 50 grid points per wavelength, and 120 intervals/period, respectively). No differences were observed.

Next, the simulation was repeated using larger 3-D disturbance amplitudes. Results of this simulation are shown in Figure 7 in the same way as in Figure 6. Apart from larger numerical noise upstream of the bubble, depicted by the high-frequency harmonics, no significant differences occur for the 2-D and 3-D waves compared to the preceding investigation. So far, no important contribution of secondary instability to the transition process could be observed for the laminar separation bubbles under investigation, even after changing the scenario from “fundamental” to “subharmonic resonance”, as reported in [4].

When looking at the amplification rates $-\alpha_i$ in Figure 8, calculated from the data shown in Figure 6, an initially rather close quantitative agreement between the DNS and LST is again observed as for the linear case in Figure 5. For clarity the 3-D α_i curves are not shown for $x > 2.0$, since α_i would overemphasize local oscillations of the amplitudes vs. x in Figure 6. Starting at $x \approx 1.85$, the amplification rates begin to deviate from LST and all waves shown turn towards a neutral behavior. The 2-D wave experiences a short distance with slightly increased amplification while the 3-D wave with the larger spanwise wave number ($\gamma = 40$) attains a rather large amplification rate before it decreases.

Comparisons with stability calculations for secondary instability at $x = 1.8$, where the 2-D disturbance amplitude is approximately 1%, yield increased 3-D amplification rates for $\gamma = 40$, thus indicating indeed a possible secondary instability just before the nonlinear saturation of the 2-D disturbances. However, identification of a secondary instability in

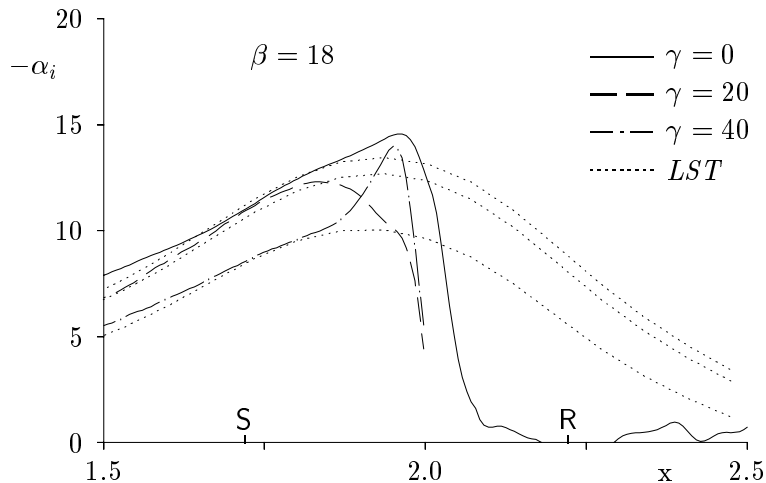


Figure 8: Comparison of DNS-amplification rates from case **F** with Linear Stability Theory (*LST*), $\beta =$ frequency, $\gamma =$ spanwise wave number.

the DNS results is very difficult in the present case due to its small difference to primary instability, as far as amplification rates are concerned. In addition, the secondary instability breaks down soon after its emergence. Similar observations are made in the subharmonic case **S** [4].

4.3.3 Oblique case

In the past years, a new 3-D amplification mechanism was found, initially in the transonic flow regime (e.g., [11]) where 3-D waves are equally or even more amplified than 2-D waves. A somewhat similar situation appears here in the separation bubble: 3-D (linear) disturbances are approximately as amplified as 2-D disturbances (cf. Fig. 4 and 5). Therefore, a 3-D instability (now called *oblique breakdown*) might be of relevance here. This possibility is investigated in case **O** by means of a pair of oblique waves with $\beta = 18$ and $\gamma = \pm 20$ (i.e., $A_k = 0$, for $k \neq 1$, and $A_1 = 10^{-5}$ in eqn. (7)).

In this case, additional nonlinear effects are expected to occur among different modes in spanwise direction. Therefore, in addition to using a finer resolution in x and t (≈ 50 grid points/wavelength, and 200 time steps/period, resp.), K in equation (6) is increased compared to the simulations above. In order to save some computer time, the beginning of the “relaminarization zone” and the end of the integration domain are placed at $x_{rz} = 2.52$ and $x_N = 3.17$, respectively. In addition, case **O** is performed as a “spatial continuation simulation” using two integration domains overlapping in downstream direction, and $K = 4$ and $K = 8$ in the two grids, respectively. Periodic inflow conditions for the disturbances calculated on the second grid beginning at $x = 1.5$, are extracted from the results of the first grid at the same x . x_0 of the first grid and the height of the integration domain in y -direction are not altered compared to the simulations discussed so far, but the number of grid points in x -direction is reduced to 498 in spite of the finer resolution.

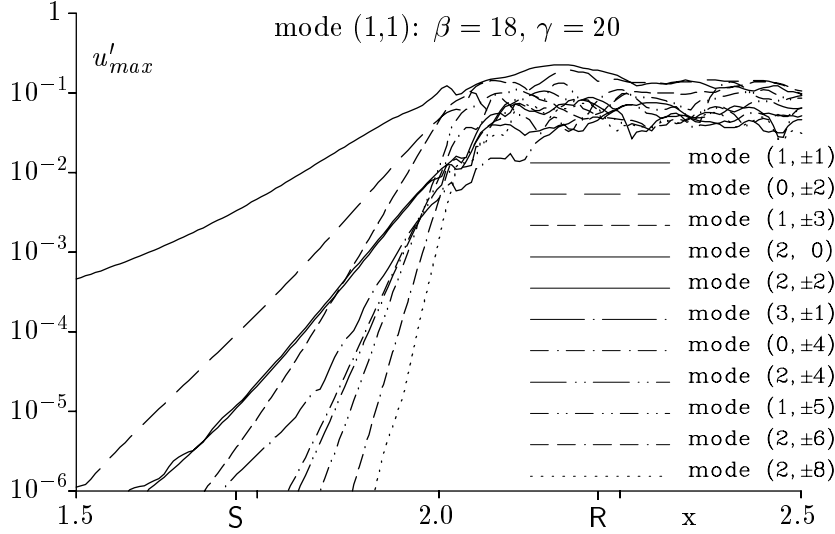


Figure 9: Amplification curves for large 3-D disturbance amplitudes (case **O**), $\beta =$ frequency, $\gamma =$ spanwise wave number.

Amplification curves u'_{max} vs. x from case **O** are shown in Figure 9 for some typical spectral modes. A typical feature of the oblique breakdown is the amplification of modes (n, k) ¹, where $n + k$ is even. These modes include 2-D disturbances, e.g., mode $(2, 0)$, and longitudinal vortices, e.g., mode $(0, \pm 2)$. The amplitudes of corresponding oblique wave pairs (denoted by $\pm k$) are added to form single curves in Figure 9. Two observations are important: first, modes $(1, \pm 1)$ are amplified according to LST until nonlinear effects lead to saturation around $x \approx 2.0$, and second, all other modes are generated by nonlinear interactions, e.g., modes $(0, \pm 2)$, $(2, \pm 2)$, and $(2, 0)$ by modes $(1, \pm 1)$. The second observation is confirmed by the amplification rates between $x = 1.5$ and $x = 2.0$ in Figure 9: the nonlinearly generated waves belonging to the interaction just mentioned, are all amplified with the same rate which is approximately twice the rate of the forcing waves. Higher-order nonlinear modes start at an initially lower amplitude with even larger amplification rates, e.g., $(1, \pm 3)$. It turns out that the local amplitudes of all nonlinearly generated modes solely depend on the local amplitude of modes $(1, \pm 1)$ [11].

In principle, the “oblique breakdown” mechanism is operative for any spanwise wave number $\gamma > 0$ as long as the corresponding oblique wave pair is amplified. From the observations in connection with case **L**, however, a “preferred” or “optimal” spanwise wave number γ_p can be expected: Decreasing γ from γ_p to $\gamma = 0$, the amplification of the 3-D waves can no longer increase, since the amplification of the 2-D wave is the largest possible, but at the same time the “oblique” mechanism somehow must decrease due to its absence in 2-D. Increasing γ beyond γ_p must also decrease the strength of the mechanism due to the reduced amplification of oblique primary waves with increasing spanwise wave number. Taking α_i of modes $(0, \pm 2)$ between $x = 1.5$ and $x = 2.0$

¹ $n =$ frequency index (relative to $\beta = 18$), $k =$ spanwise wave number index (relative to $\gamma = 20$).

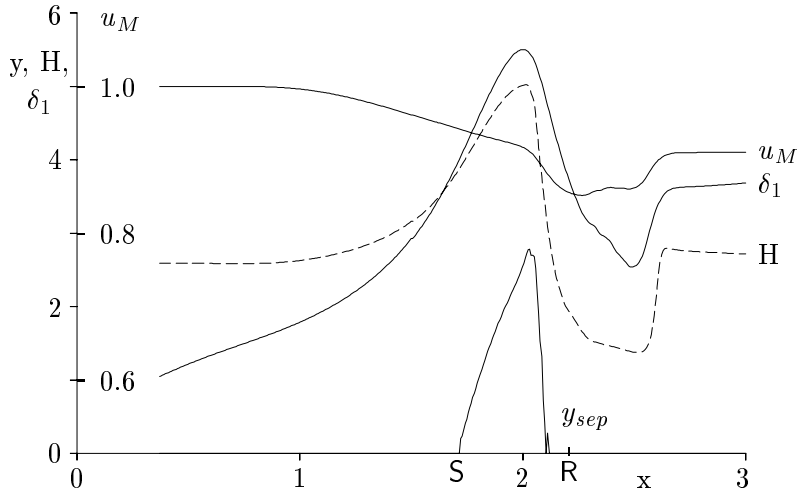


Figure 10: 2-D mean-flow parameters in case **O**: free-stream velocity u_M , shape factor H , displacement thickness δ_1 , separation streamline y_{sep} . **S**, **R**: separation and reattachment of the undisturbed base flow.

as a reference, a number of test calculations were performed using different (global) spanwise wave numbers γ in eqn. (6), and the largest amplification of modes $(0, \pm 2)$ was found near $\gamma_p \approx 20$. The “preferred” spanwise wavelength of the longitudinal vortices represented by modes $(0, \pm 2)$ ($\gamma \approx 40$) is thus $\lambda_{zp} \approx 0.157$. With $\delta_{1s} \approx 4$ from Figure 3, λ_{zp} can be expressed as $\lambda_{zp} \approx 12.4\delta_{1s}$, when the stretching in y -direction by \sqrt{Re} is taken into account.

As already observed in case **F**, additional nonlinear effects lead to the saturation of all disturbance amplitudes at $x > 2.0$. Although the resolution is still not adequate to resolve all aspects of the flow in that region, a number of interesting qualitative mean-flow features can be observed, as will be shown in the next two figures.

The downstream development of the free-stream velocity u_M , the shape factor H , the displacement thickness δ_1 , and the separation streamline y_{sep} for the mean flow from case **O** are given in Figure 10 for comparison with the base flow (i.e., the undisturbed steady flow) in Figure 3. No differences occur for $x < 1.85$ in agreement with the small disturbance amplitudes observed further above. In the rearward part of the bubble, however, everything is different from the undisturbed flow: Reattachment occurs earlier, the bubble’s outline resembles a triangle, the shape factor and the displacement thickness both decrease to very low values, and even the free-stream velocity is decreased. The retardation of the outer flow is thus increased by additional 5% relative to U_∞ by the action of the disturbances, which have reached such a large amplitude that they have finite amplitude at y_M , despite their exponentially fast decay with increasing y . Such a large change of the velocity at the upper boundary of the integration domain could cause undue influences of the chosen height of the domain

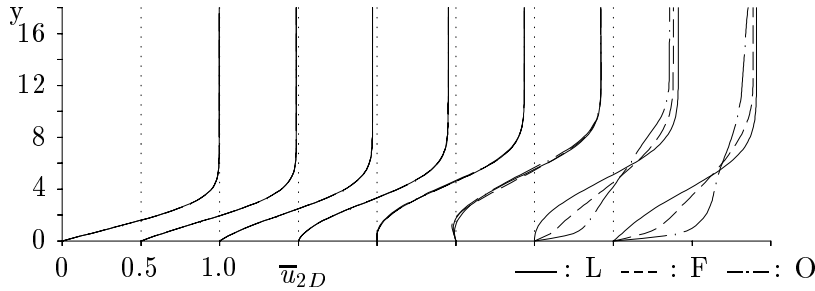


Figure 11: Comparison of 2-D mean-flow profiles at $x = 1.0, 1.2, 1.4, \dots, 2.4$.

on the flow, especially for $x > 2.1$. This would be clarified by additional simulations using different distances y_M of the upper boundary from the flat plate. Other investigations using a viscous-inviscid interaction model of the kind proposed in [12] are also of interest, they would further remove possible effects of a finite height of the integration domain.

The sudden jump of all curves back to the undisturbed values at $x \approx 2.52$, however, is due to the artificial suppression of the disturbances in the “relaminarization zone” beginning at $x_{rz} = 2.52$. This shows the efficiency of the “relaminarization zone”. Compared to case **L**, and to the influence of the bubble on the base flow described in connection with Figure 3, where only a local influence of the bubble on the flow was observed, the influence of the large-amplitude disturbances is not local, since, once amplified and saturated, a quasi-turbulent flow would persist for all x downstream of the bubble if no relaminarization were enforced.

The downstream evolution of the 2-D mean-flow profiles for the three cases **L/F/O** are compared in Figure 11. For $x < 2.0$, there is no difference due to the small disturbance amplitudes. Further downstream in the reattachment zone, the most striking differences appear: the profiles according to cases with large-amplitude disturbances have different curvature and a much larger $\partial u/\partial y$ close to the wall. Qualitatively these profiles look like turbulent boundary layer profiles, and indeed, calculation of the shape factor H in the reattachment zone for the nonlinear cases yields $H \approx 2.0$, and $H \approx 1.4$ in case **F**, and **O**, respectively. Thus, the qualitative and quantitative resemblance of the mean flow behind the bubble to a turbulent mean flow is most pronounced in case **O** (a typical shape factor for turbulent flat-plate boundary layers is $H \approx 1.5$). The apparent difference between case **F** and case **O** is due to different 3-D disturbance amplitudes: the flow in case **F** is dominant 2-D and therefore qualitatively more distinct from 3-D turbulence than in case **O**.

In summary, the separation bubble in case **O** yields the best qualitative agreement with a transitional laminar separation bubble. In addition, longitudinal vortices which have already been observed in experiments (e.g., [2]) might be due to the occurrence of modes $(0, \pm 2)$. The calculation of λ_{zp} further above gives an estimate for the spanwise wavelength of such

vortices. What happens to case **O** if an even large amplitude 2-D disturbance is present, is investigated in the next section.

4.3.4 *Combined case*

The results presented in sections 4.3.2, and 4.3.3 show that a large amplitude 2-D disturbance will not immediately drive small amplitude 3-D disturbances to large-amplitude saturation, the mutual interaction of 3-D disturbances seems to be much better suited for that purpose, instead. A problem with case **O**, however, is that the flow is dominated by 3-D disturbances whereas experiments show a dominance of 2-D effects.

Until reliable receptivity studies are available, the initial disturbance spectrum must be estimated and different generic combinations must be investigated, as it is done here. Due to the convective nature of the instabilities observed above, the flow downstream of the separation bubble depends on the disturbance spectrum introduced further upstream. In order to check the relevance of case **O**, a number of additional simulations were performed, where large-amplitude subharmonic, fundamental or higher harmonic 2-D disturbances were added to the initial 3-D disturbance in case **O**. The most “dangerous” combination found, was that using fundamental disturbance frequency, since that frequency is the only one that is comparably amplified as the forcing 3-D modes $(1, \pm 1)$ already in the “linear region” upstream of the bubble.

The simulation presented in this section is performed using ≈ 50 grid points/wavelength, 200 time steps/period, $\gamma = 20$, $K = 4$ in equation (6), and 594 grid points in x . Disturbances are generated with $\beta = 18$, $A_0 = 1.1 \cdot 10^{-5}$, and $A_1 = 10^{-5}$ in eqn. (7), and x_0 and the height of the integration domain are left unchanged compared to the simulations already described. The amplitudes A_0 and A_1 are chosen so that mode $(1,0)$ and the superposition of mode $(1,1)$ with mode $(1,-1)$ start with equally large disturbance amplitudes at the disturbance strip.

Amplification curves for the new simulation (case **C**) are presented in Figure 12. Figure 12(a) contains only those (even) modes (n,k) which are also present in case **O** with the results from Figure 9 replotted as dotted lines. Compared to case **O**, some modes (e.g., $(2,0)$ and $(3, \pm 1)$) are initially larger while others remain unchanged until $x \approx 1.85$. Downstream of this x -station, the even modes are generally smaller than in case **O**, this is especially apparent for the longitudinal vortex modes $(0, \pm 2)$ and obviously due to the presence of large-amplitude odd modes shown in Figure 12(b). For $x > 1.85$ two major qualitative differences between case **C** and case **O** arise from the quantitative differences observed further upstream: (i) the flow is dominated by the 2-D wave $(1,0)$ in a manner qualitatively similar to that in case **F**, and (ii) the longitudinal vortices are represented by modes $(0, \pm 1)$ instead of modes $(0, \pm 2)$, i.e., their spanwise wavelength is halved.

As already observed in case **O** (Figure 9), some modes are again equally amplified between $x = 1.5$ and $x = 2.0$, e.g., modes $(0, \pm 2)$, $(2,0)$, and $(2, \pm 2)$ in Figure 12(a), and modes

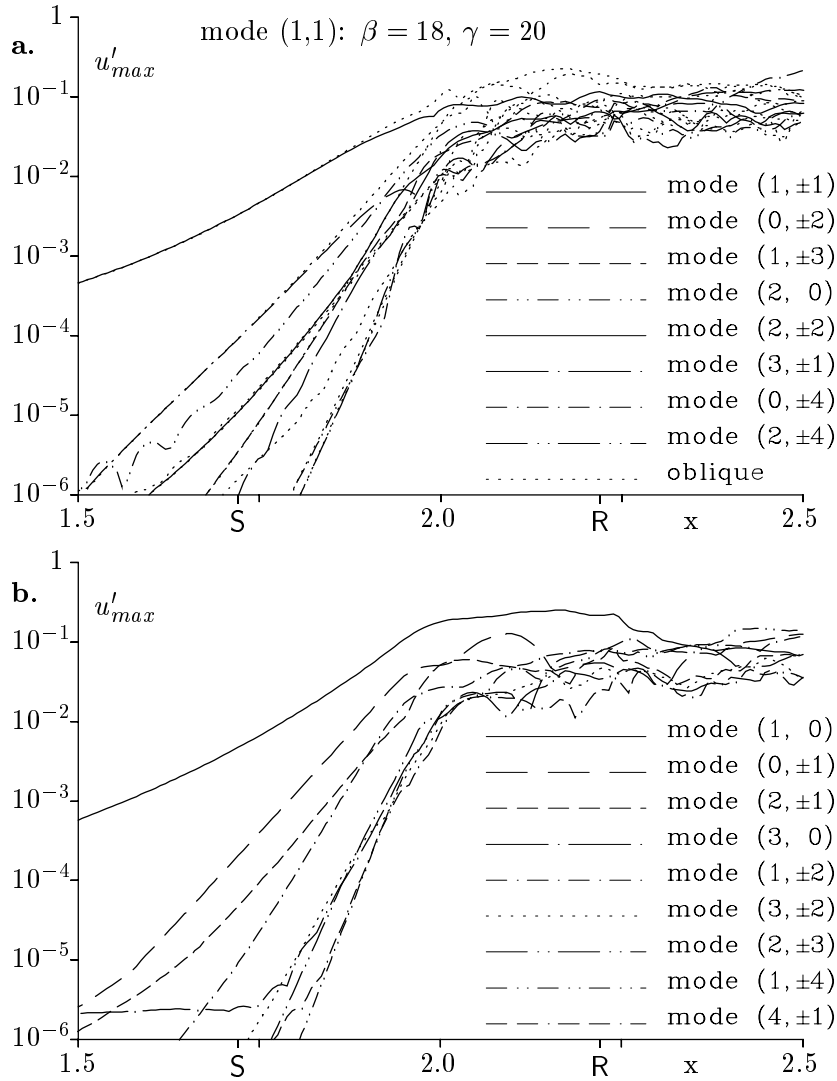


Figure 12: Amplification curves for large 2-D and 3-D disturbance amplitudes (case C). (a.) $n+k$ even, (b.) $n+k$ odd. Dotted lines in (a) represent the results already shown in Figure 9.

$(0, \pm 1)$ and $(2, \pm 1)$ in Figure 12(b). Such wave pair triples or pairs thus belong to the same nonlinear combination interaction mechanism, i.e., mode $(1, 1)$ with its complex conjugates in the first case, and mode $(1, 0)$ with modes $(1, \pm 1)$ in the second case. Even the increased amplitudes of some modes (e.g. $(2, 0)$) can be explained by wave (mode) interaction: compared to case **O**, where it is generated solely by $(1, 1)$ and $(1, -1)$, a self interaction of mode $(1, 0)$ also contributes to this mode in case **C** and provides for an increased amplitude.

Although the even modes in case **C** are somewhat smaller than in case **O** for $x > 1.85$, and despite the existence of odd modes, the underlying instability mechanism appears to be the same. Namely, the nonlinear interaction of modes in the frequency-spanwise-wave-number-spectrum. Thus, the inclusion of 2-D disturbances into the “oblique breakdown” model does not alter the principle found there.

5. CONCLUSIONS

Inclusion of 3-D disturbances in the DNS of an arbitrarily chosen laminar separation bubble gave a number of unexpected results. Since only one specific base-flow configuration has been investigated so far, it is not yet clear to what extent the present results may be generalized. Further investigations using other base flow parameters, e.g., larger free-stream velocity drop Δu_M , larger Reynolds number at separation $Re_{\delta_1 S}$, larger integration domain in y-direction, etc. are therefore necessary.

6. ACKNOWLEDGEMENTS

Without the financial support provided by the Deutsche Forschungsgemeinschaft (DFG) under contract Ri 680/1-1 and by the University of Stuttgart, the present investigations would not have been possible. The support of both institutions is therefore greatly appreciated. Special thanks go to Wolfgang Müller for taking the “burden” of attending the conference and presenting part of the present results, while the first author was sick.

7. REFERENCES

References

- [1] Muller, T.J. (ed.), “Low Reynolds Number Aerodynamics”, Springer Lecture Notes in Eng., Springer, New York, 1989.
- [2] Althaus, D., “Drag measurements on airfoils”, XVII OSTIV-Congress, Paderborn, Germany, 1981.
- [3] Gruber, K., Bestek, H. and Fasel, H., “Interaction between a Tollmien-Schlichting wave and a laminar separation bubble”, AIAA Paper 87-1256, 1987.
- [4] Rist, U., “Nonlinear effects of 2-D and 3-D disturbances on laminar separation bubbles”, *in* S.P. Lin (ed.), Proc. “IUTAM-Symp. Nonlin. Instab. of Nonpar. Flows”, Springer, New York, 1994, pp 324–333.
- [5] Fasel, H., Rist, U. and Konzelmann, U., “Numerical investigation of the three-dimensional development in boundary layer transition”, AIAA J., 28, 1, January 1990, pp 29–37.

- [6] Kloker, M., Konzelmann, U. and Fasel, H., “Outflow boundary conditions for spatial Navier-Stokes simulations of transitional boundary layers”, *AIAA J.*, *31*, 4, May 1993, pp 620–628.
- [7] Kloker, M., “Direkte Numerische Simulation des laminar-turbulenten Strömungsumschlages in einer stark verzögerten Grenzschicht”, Dissertation Universität Stuttgart, 1993.
- [8] Rist, U. “Numerische Untersuchung der räumlichen, dreidimensionalen Störungsentwicklung beim Grenzschichtumschlag”, Dissertation Universität Stuttgart, 1990.
- [9] Rist, U. and Fasel, H., “Direct numerical simulation of controlled transition in a flat-plate boundary layer”, submitted to *J. Fluid Mech.*, September 1993.
- [10] Herbert, Th., “Secondary instability of boundary layers”, *Ann. Rev. Fluid Mech.*, *20*, 1988, pp 487–526.
- [11] Thumm, A., “Numerische Untersuchungen zum laminar-turbulenten Strömungsumschlag in transsonischen Grenzschichtströmungen”, Dissertation Universität Stuttgart, 1991.
- [12] Veldman, A.E.P., “New, quasi-simultaneous method to calculate interacting boundary layers”, *AIAA J.*, *19*, 1, January 1981, pp 79–85.

36-1

36-2

36-3

36-4

36-5

36-6

36-7

36-8

36-9